CHAPTER 11

Pulsed Photothermal Radiometry of Inhomogeneous Tissue

Scott Prahl

Oregon Medical Laser Center
Portland, Oregon 97225 U.S.A.

1. INTRODUCTION

This chapter describes a technique for extracting an internal thermal profile using measurements of the surface temperature. The method is applicable to materials and tissues with uniform thermal properties and non-uniform optical properties. The technique is based on singular value decomposition and works reasonably well down to depths of about 500 μm. The uncertainty in the location of the internal temperature layers grows linearly with the depth of the layer. The inversion algorithm is tested using computer simulations and experiments on colored glass. Analysis of *in vivo* data from a tanning experiment on human skin is presented to show the potential of the technique. Biological systems are typically characterized by complex structures. Despite this, physicists and engineers usually assume uniform properties when optically modelling such systems. Analytic solutions are mathematically tractable only when the model contains one, two or three layers, and often the properties of these layers must be known before the method can be used. Unfortunately, real biological samples are not very uniform and one has no *a priori* knowledge of the optical properties. For example, the skin is composed of many layers: a thin stratum corneum resting on the epidermis that in turn sits on the dermis; blood vessels, hair follicles, and melanin granules may be distributed throughout these layers.

The efficacy of photobiological or photoprotective therapies depends on light absorption. Because the wide variation in composition and thickness of the layers in human skin makes the exact distribution of absorbed light impossible to predict, it would be useful to have a method to measure this distribution. Some practical

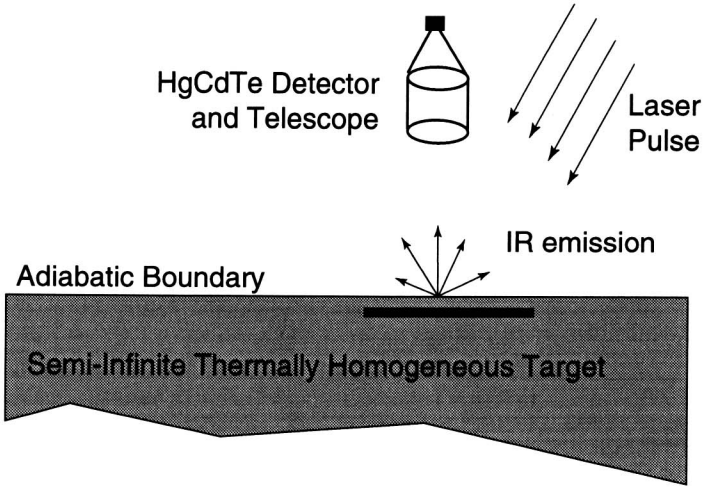

FIGURE 1. The PPTR problem. A laser pulse thermally perturbs a semi-infinite material. The sample is thermally homogeneous but optically inhomogeneous. The surface temperature is measured using an infrared detector.

applications in dermatology of such a technique include providing diagnostic feedback for the treatment of pigmented lesions (e.g., port wine stains), monitoring changes in thickness and concentration of topically applied medicines over time, providing diagnostic information to improve the treatment of psoriasis, and studying the photoprotective mechanisms of skin.

Pulsed photothermal radiometry (PPTR) uses pulsed flashes of light (typically achieved using a pulsed dye laser) to create a temperature perturbation (Fig. 1). The surface temperature is monitored with an infrared detector. An important advantage of PPTR over other methods is that the measurement is made without touching the sample. For example, simply resting a probe on the surface of the skin for several seconds will change the hydration characteristics of the stratum corneum [1]. Slightly heavier contact will change the blood flow to the area under the probe, and is readily seen as blanching of the skin.

PPTR has been used extensively with non-biological materials (e.g., rubber, plastics, pigments, powders) [2-7]. The technique has been used on biological samples to determine surface absorption properties by using the temperature increase immediately following the laser pulse in arteries [8], biliary calculi [9], and skin [10]. PPTR of laminated materials (and skin) was presented by Balageas [11]. Long *et al.* investigated the subsurface absorption phenomena arising from bruised human skin *in vivo* using a simple two-layer absorption model [12]. This work was recently

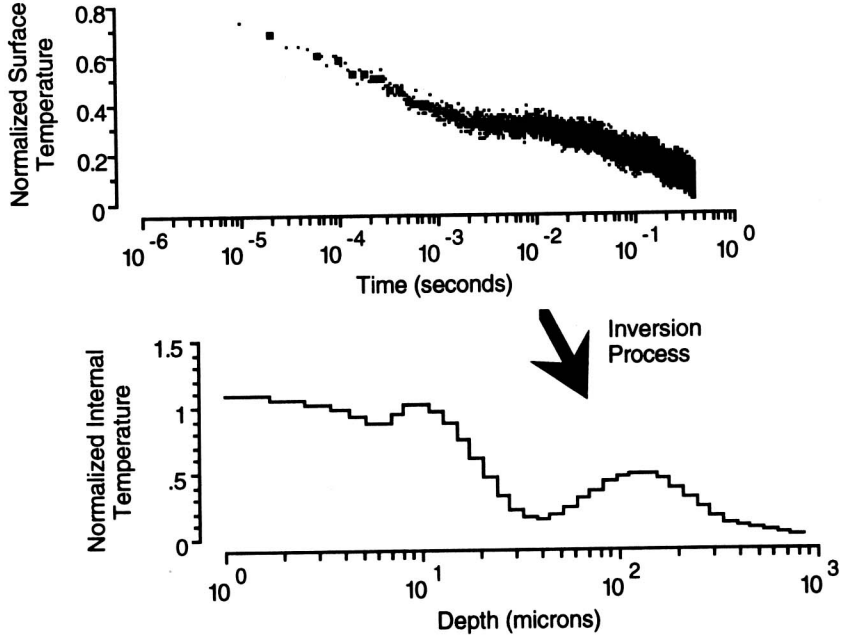

FIGURE 2. The inversion problem. The goal is to convert surface temperatures as a function of time to initial temperatures as a function of depth after the laser pulse.

extended to a two-layer scattering and absorbing model that more accurately simulated skin [13]. These studies all require relatively simple absorption geometries — typically homogeneous but perhaps having as many as four layers. The dimensions of these layers must be known before the PPTR signal may be interpreted. Furthermore, when scattering is present, many of the models become inapplicable.

1.1 The Problem

The problem is summarized by Figure 2. How can the detected thermal signal be converted into an initial temperature distribution without knowing the location and magnitude of the internal light absorbers? Some assumptions must be made: in particular, the sample is assumed to be semi-infinite and to have uniform thermal properties. The thermal boundary condition at the surface is assumed to be adiabatic and the problem is constrained to be one-dimensional.

The technique is based on the following physical argument [14,15]. The initial surface temperature, immediately after the flash, depends only on the initial temperature at the surface. After a short time (say 5 ms), thermal effects can only propagate a short distance ($\approx$5 μm). Therefore the surface temperature 5 ms after the pulse will only be influenced by the initial temperatures at the surface and those in the sample down to a depth of about 5 μm. Since the initial surface temperature is known, the initial temperature of a thin layer just below the surface can be determined. Repeating this process allows mapping of the entire initial temperature distribution (or light absorption) distribution. Jacques *et al.* developed an iterative algorithm based on the above principle and applied it to port wine stain lesions of human skin [15].

The algorithm described in this chapter uses a matrix formulation to solve the problem directly. The effect of infrared absorption from points within the sample is also incorporated into this analysis. Finally, the technique is evaluated using data from known thermal distributions (both simulated and measured). The limitations on this technique are that absorption profiles only down to a depth of 500 μm can be made before the signal decays too much. Fortunately, this range covers the tissue structures that comprise the majority of the interesting structures of the skin—the stratum corneum, the epidermis, and the basal cell layer.

2. THEORY

This section formulates the problem of converting a series of surface temperature measurements to an initial temperature distribution as an integral equation. The appropriate corrections necessary for infrared penetration are included. The integral equation is converted to a least squares matrix problem.

2.1 The Integral Equation

The integral equation is obtained by convolving the appropriate Green's function for thermal propagation with an arbitrary source distribution. The derivation is complicated somewhat by introducing the changes necessary to account for finite infrared penetration of light in the sample. The problem is considered one-dimensional both optically and thermally. Practically, this requires that the laser spotsize should be relatively large (say 5 mm in diameter) so that at the center the optical and thermal radial diffusion is negligible.

The change in the backscattered radiometric signal $S(t)$ is obtained by integrating the black-body radiation from all sites within the sample weighted by a suitable attenuation factor. If the temperature after the laser pulse is $T(z,t)$ and the infrared absorption coefficient averaged over the detection spectral bandwidth is μ_{IR}, then the backscattered radiometric signal is [2],

$$S(t) = \eta a_D \epsilon \sigma \int_0^\infty [T(z,t)^4 - T_0^4] \exp(-\mu_{IR} z) \mu_{IR} dz. \qquad (1)$$

In this equation T_0 is the uniform unperturbed sample temperature, η is the detector efficiency (incorporating both the sensitivity and collection efficiency of the detector), a_D is the detector area, ϵ is the emissivity of the sample, and σ is the Stefan-Boltzmann constant. The detector efficiency η, the emissivity ϵ, and the absorption coefficient μ_{IR} are all wavelength dependent; average values over the wavelength range of the infrared detector must be used.

If the temperature rise following the laser pulse $T(z,t)$-T_0 is small[1] the bracketed quantity in Eq. (1) can be expanded using the binomial theorem. Neglecting terms of $O([T(z, t) - T_0]^2)$ and higher yields

$$S(t) = 4\eta a_D \sigma \epsilon T_0^3 \int_0^\infty [T(z,t) - T_0] \exp(-\mu_{IR} z) \mu_{IR} dz \qquad (2)$$

The temperature at any time following the laser pulse is a convolution of the appropriate Green's function with the initial thermal distribution [16],

$$T(z,t) - T_0 = \int_0^\infty T(z',0) G(z', t' = 0; z, t) dz' \qquad (3)$$

where $T(z', 0)$ is the temperature immediately after the laser pulse. $G(z', t'; z, t)$ is the Green's function for an instantaneous planar source of heat located at a depth z' and released at time t'.

---

[1] Typical temperature increases for biological problems are one to ten degrees Celsius.

The infrared absorption coefficient μ_{IR} determines the depth that the infrared detector sees into the sample[2]. The infrared absorption coefficient provides a natural length scale for this problem. A non-dimensional time and length may be defined as

$$\zeta \equiv \mu_{IR} z \qquad \text{and} \qquad \tau \equiv \mu_{IR}^2 \kappa \, t \tag{4}$$

where κ is the thermal diffusivity. A normalized radiometric signal $s(\tau)$ can be written in terms of the dimensionless parameters τ and ζ substituting Eq. (3) into Eq. (2)

$$s(\tau) = \frac{S(t)}{4\eta a_D \sigma \epsilon T_0^3} = \int_0^\infty \left[\int_0^\infty T(\zeta',0) G(\zeta',0;\ \zeta,\tau) d\zeta' \right] \exp(-\zeta) d\zeta . \tag{5}$$

Green's function may be combined with the infrared penetration effect by formally interchanging the order of integration in Eq. (5)

$$s(\tau) = \int_0^\infty T(\zeta',0) \left[\int_0^\infty G(\zeta',0;\ \zeta,\tau) \exp(-\zeta) d\zeta \right] d\zeta' . \tag{6}$$

An inhomogeneous Fredholm integral equation of the first kind follows immediately as

$$s(\tau) = \int_0^\infty f(\zeta) K(\zeta,\tau) d\zeta \tag{7}$$

where the initial temperature distribution has been redefined as

$$f(\zeta) \equiv T(\zeta,0) \tag{8}$$

The kernel $K(\zeta',\tau)$ in Eq. (7) is

$$K(\zeta',\tau) = \int_0^\infty G(\zeta',0;\ \zeta,\tau) \exp(-\zeta) d\zeta \tag{9}$$

2.2 The Matrix Approximation

The first-order Fredholm integral Eq. (7) is solved by approximating the integral

---

[2] The weighted infrared absorption coefficient for water using the 8-12 μm detector of this chapter was μ_{IR} = 1200 cm^{-1}. The infrared penetration was therefore about 8 μm.

as a sum and then identifying the resulting matrix equation as a classic least-squares problem. The integral for the surface temperature may be approximated by

$$s(\tau) \approx \sum_{i=1}^{N} K(\zeta_i,\tau)\, f(\zeta_i)\Delta\zeta_i \tag{10}$$

where $\Delta\zeta_i = \zeta_{i+1} - \zeta_i$. The initial temperature distribution in the sample has been approximated by N discrete points. The sum (10) is exact as $\Delta\zeta_i \to 0$ and $N \to \infty$. The final step in the discretization process is to select a particular time τ_j for the surface temperature,

$$s(\tau_j) \approx \sum_{i=1}^{N} K(\zeta_i,\tau_j)\, f(\zeta_i)\, \Delta\zeta_i \tag{11}$$

The normalized radiometric signal from the sample is characterized by the vector **s** with individual entries $s(\tau_j)$, the kernel **K** with entries $K(\zeta_i,\tau_j)$, and internal temperatures **f** with entries $f(\zeta_i) = T(\zeta_i, 0)$. If the number of sampled surface temperatures is M, then **s** has length M and the kernel **K** will be a $M \times N$ matrix. In matrix notation, the integral equation (7) is

$$\mathbf{s} = \mathbf{Kf} \tag{12}$$

Typically, the number of radiometric measurements M greatly exceeds the number of internal temperatures N that will be found. Equation (12) is a least-squares type of problem, in which it is desired to find the best N internal temperatures for a set M of surface measurements.

2.3 Kernels

All the physics of the thermal interaction is contained in the kernel. In this section, a closed-form solution for the kernel characterizing radiation from a uniformly heated layer in a semi-infinite medium with adiabatic boundaries and constant thermal properties is found.

Green's function for a planar instantaneous source at time $\tau = 0$ and depth ζ' is [16]

$$G(\zeta',\tau' = 0;\, \zeta,\tau) = \frac{Q}{2\sqrt{\pi\tau}}\left[\exp\left(-\frac{(\zeta-\zeta')^2}{4\tau}\right) + \exp\left(-\frac{(\zeta+\zeta')^2}{4\tau}\right)\right] \tag{13}$$

where Q is a unit of heat deposited at sources located at ζ' and - ζ'. Substituting this expression into Eq. (9) and integrating yields

$$K_{\text{plane}}(\zeta,\tau) = \frac{1}{2}\exp(\tau-\zeta)\operatorname{erfc}\left(\sqrt{t}-\frac{\zeta}{2\sqrt{t}}\right)+\frac{1}{2}\exp(\tau+\zeta)\operatorname{erfc}\left(\sqrt{\tau}+\frac{\zeta}{2\sqrt{\tau}}\right) \quad (14)$$

where erfc (x) is the complementary error function. The kernel is plotted for various values of ζ and τ in Figure 3.

The kernel for a plane source could be used in the inversion process. However the initial temperature distribution inside a real sample does not consist of a series of distributed delta-function sources. A more realistic model would be one that simulated the internal distribution as a set of layer sources. To obtain the appropriate kernel for a layer source with finite thickness, then the kernel for a planar source, Eq. (14), must be integrated over the extent of the layer.

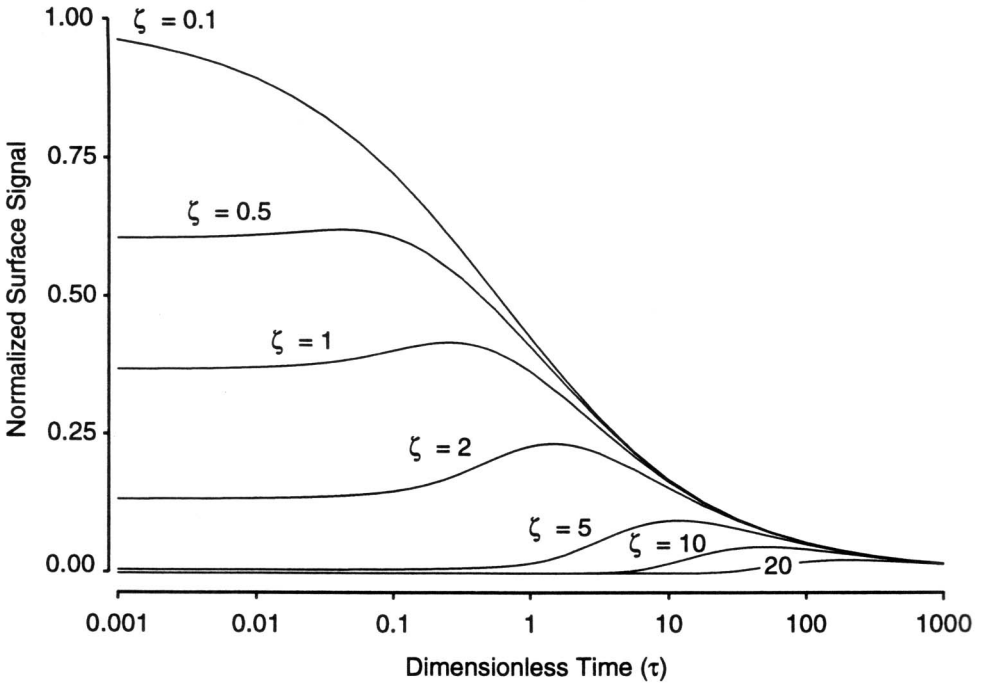

FIGURE 3. The kernel of equation (12). When the infrared penetration is non-zero then some signal reaches the surface immediately even when the source is located below the surface. For water, $\tau = 0.001$ corresponds to approximately half a microsecond.

If the top of the layer is located at ζ_i, and the bottom of the layer is at ζ_{i+1} then

$$K_{ij} = \int_{\zeta_i}^{\zeta_i+1} K_{\text{plane}}(\zeta,\tau)\,d\zeta = h(\zeta_{i+1},\tau_j) - h(\zeta_i,\tau_j) \tag{15}$$

where

$$h(\zeta,\tau) = \text{erfc}\left(\frac{\zeta}{2\sqrt{\tau}}\right) \frac{1}{2}\exp(\tau-\zeta)\,\text{erfc}\left(\sqrt{\tau}-\frac{\zeta}{2\sqrt{\tau}}\right) + \frac{1}{2}\exp(\tau+\zeta)\,\text{erfc}\left(\sqrt{\tau}+\frac{\zeta}{2\sqrt{\tau}}\right) \tag{16}$$

The kernel defined by Eq. (15) was used in all calculations in this paper. When $i = N$ then $\zeta_{i+1} \to \infty$ i.e., all the signal reaching the surface from points ζ_i and deeper is lumped together into the Nth layer.

Clearly, if Eq. (10) is a poor approximation to the true integral, then any solution based on this sum will also be poor. One convenient consequence of using layers for the kernel is that in the special case $f(\zeta) = 1$

$$\sum_{i=1}^{N} K_{ij}\Delta\zeta_i \equiv \int_0^{\infty} K(\zeta,\tau)\,d\zeta \tag{17}$$

for any number of points N and for any time τ.

3. ANALYSIS

This section presents a numerical solution to the inverse heat transfer problem. The integral equation is solved by approximating the kernel, based on a Marquardt-Levenberg analysis. The difficulties associated with a first-order Fredhom integral equation are mitigated somewhat through careful selection of the times for the measured signal and the depths for the calculated initial temperature.

3.1 Matrix Solution

The least squares problem of Eq. (12) is formally solved by writing

$$\mathbf{f} = \mathbf{K}^{-1}\mathbf{s} \tag{18}$$

where the pseudo-inverse $\mathbf{K}^{-1}$ is based on rewriting $\mathbf{K}$ as

$$\mathbf{K} = \mathbf{u}^T\mathbf{m}\mathbf{v} \tag{19}$$

using singular value decomposition. Here $\mathbf{u}$ and $\mathbf{v}$ are two row orthonormal matrices and $\mathbf{m}$ is a diagonal matrix. The pseudo-inverse is defined as

$$\mathbf{K}^{-1} = \mathbf{v}^T\mathbf{m}^{-1}\mathbf{u} \tag{20}$$

The initial internal temperature distribution $\mathbf{f}$ is then

$$\mathbf{f} = \mathbf{v}^T\mathbf{m}^{-1}\mathbf{u}\mathbf{s} \tag{21}$$

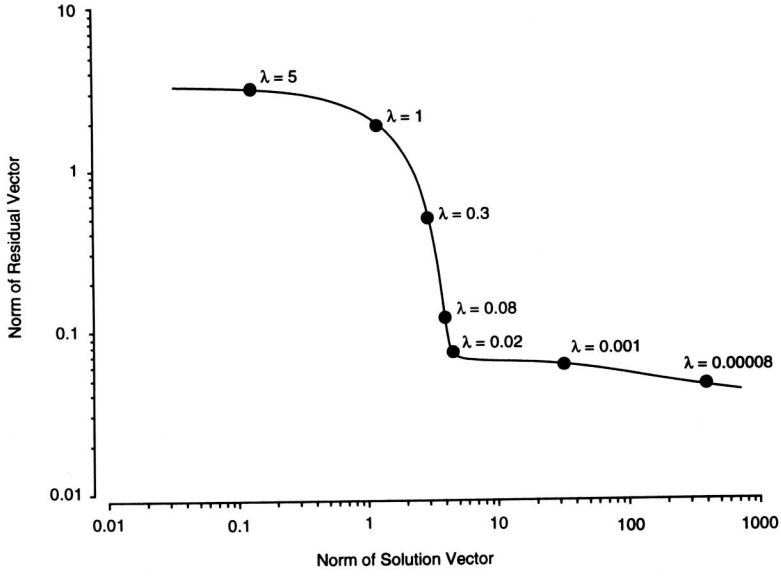

FIGURE 4. Marquardt-Levenberg analysis of the data shown in Figure 2. As λ decreases, better and better approximations of the measured data are achieved. However, the magnitude of the predicted internal temperature increases as well. Clearly, reducing λ past the knee in the curve does not dramatically increase the accuracy of the approximated initial data (i.e., reduce the magnitude of the residual).

The entries in the matrix **m** are the singular values of the matrix **K**. These can be arranged to be non-increasing, and if the rank of **K** is k then exactly k entries will be positive. The complete set of singular values m_i is required to satisfy the equality in Eq. (19). However, good approximations of **K** can be achieved by leaving out values of m_i that are small. Omitting the small singular values is important because these small values are associated with large $1/m_i$ entries in the diagonal matrix $\mathbf{m}^{-1}$. Since the inverse matrix $\mathbf{m}^{-1}$ multiplies the measured surface temperature, these small singular values will cause huge changes in the calculated initial temperatures.

The goal, then, is to approximate the kernel sufficiently well that all the relevant physics is retained, and yet find an approximation that prevents the small singular value entries from amplifying the noise in the surface measurements. One solution is to replace all the very small singular value entries $1/m_i$ by zero. Another, more systematic method is to use a Marquardt-Levenberg analysis that smoothly attenuates small singular values by introducing a parameter λ. The singular values are replaced by terms with the form $\sqrt{m_i^2 + \lambda^2}$. This creates new matrices and vectors that satisfy

$$\mathbf{f}_\lambda = \mathbf{K}_\lambda^{-1}\mathbf{s}_\lambda \tag{22}$$

and approximate the originals with increasing fidelity as $\lambda \to 0$. The details of one Marquardt-Levenberg implementation, including computer source code, are given in Lawson and Hanson [17].

A graphical representation of the consequences of various approximations of the kernel is shown in Figure 4. The horizontal axis is the norm of the solution vector $\| \mathbf{f}_\lambda \|$; this norm will increase as the solution oscillates more and more. The vertical axis represents the norm of the difference between the measurements and approximation to the measurements i.e., $\| \mathbf{s} - \mathbf{s}_\lambda \|$.

3.2 Selecting Times and Depths

To understand how often the surface temperature should be sampled consider a plane source located at a depth ζ. The characteristic time τ_c it takes for heat from a planar source to reach the surface can be estimated as the time of maximum temperature at the surface. For simplicity, if both the adiabatic boundary condition at the surface and the infrared penetration are ignored, then the change in temperature following an instantaneous plane source of heat at $\tau = 0$ and at a depth ζ will be

$$\Delta T(\tau) = \frac{Q}{2\sqrt{\pi\tau}} \exp\left[\frac{-\zeta^2}{4\tau}\right] \tag{23}$$

The time at which the maximum occurs is,

$$\tau_c = \frac{\zeta^2}{2} \tag{24}$$

Therefore the interval between thermal maxima from two sources at depths ζ and $\zeta + \Delta\zeta$ can be characterized as

$$\Delta\tau_c = \zeta\Delta\zeta + \frac{(\Delta\zeta)^2}{2} \tag{25}$$

For any fixed separation $\Delta\zeta$, the temporal shift will be smallest when $\zeta = 0$ (i.e., the two sources are close to the surface). The sampling theorem says that the sampling rate must be at least twice as fast to resolve individual sources. Therefore the smallest distance between sources that can theoretically be resolved using a surface temperature measurement lasting $\Delta\tau_c$ is

$$\Delta\zeta_{min} \approx \sqrt{2\Delta\tau_c} \tag{26}$$

To achieve one micrometer resolution in water, the minimum sampling time must be 3 μs. A 10 μm resolution requires a minimum sampling time of 300 μs. Typically, these times are much longer than the sampling times characteristic of a PPTR experiment. The above relation is primarily useful for determining the location of the first depth $\zeta_1 = \Delta\zeta_{min}$.

If the sampling time for each surface measurement is $\Delta\tau_{samp}$, then the number of samples made during a time $\Delta\tau_c$

$$n = \frac{\Delta\tau_c}{\Delta\tau_{samp}} \approx \frac{\zeta\Delta\zeta}{\Delta\tau_{samp}} \tag{27}$$

where the approximation is valid for deeply buried sources ($\zeta >> \Delta\zeta$). The number n is the total number of samples that can be averaged and still retain the ability to localize a source at a depth ζ. Since the depth of a source is closely related to time, the number of samples that can be averaged at a particular time τ_c can be obtained by substituting $\zeta = \sqrt{2\tau_c}$ into Eq. (27)

$$n \approx \frac{\sqrt{2\tau_c}\Delta\zeta}{\Delta\tau_{samp}} \quad . \tag{28}$$

Therefore the number of samples that can be averaged increases as the square root of the time. Furthermore, the number of samples increases linearly with the separation $\Delta\zeta$.

If the resolution of a single measurement is ΔS (normalized to the input irradiance), then n measurements will improve the resolution to $\Delta S'$

$$\Delta S' = \frac{\Delta S}{\sqrt{n}} \tag{29}$$

Therefore the resolution of measurements will improve as the fourth root of time when the number of samples averaged is determined using Eq. (28)

$$\Delta S' \sim \Delta S(\Delta\zeta)^{-1/2}\tau^{-1/4} \tag{30}$$

Unfortunately, the improvement in resolution gained by averaging more and more samples is not great enough to significantly increase the useful depth of penetration. For example, say that the initial signal (after averaging) from a source 1 μm deep is ten times the intrinsic detector resolution. The improvement in signal for a source at depth ζ_2 will be

$$\frac{\sqrt{n_1}}{\sqrt{n_2}} = \left[\frac{\tau_2}{\tau_1}\right]^{1/4} = \left[\frac{\zeta_2}{\zeta_1}\right]^{1/2} \tag{31}$$

If $t_1 = 1$ μs and $t_2 = 100$ ms ($z_1 \approx 0.4$ μm and $z_2 \approx 100$ μm), then

$$\frac{\sqrt{n_1}}{\sqrt{n_2}} = \left[\frac{10^{-1}}{10^{-6}}\right]^{1/4} \approx 20 \tag{32}$$

or the thermal resolution at 100 ms will be about 20 times better than the thermal resolution at 1 μs. If the signal reaching the surface from the 100 μm source were equal to the signal from the 1 μm source then the last averaged temperature measurement would be about two hundred times the detector resolution. The maximum signal for later times (and therefore depths) decreases rapidly. The maximum temperature is

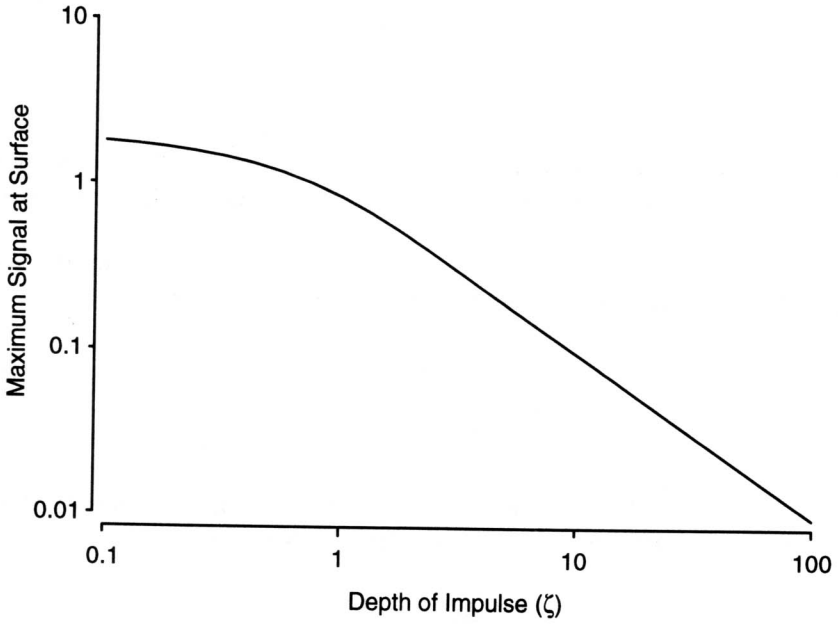

FIGURE 5. The maximum surface temperature for impulses located at various depths. Note the maximum signal drops an order of magnitude as the depth of the pulse changes from ζ=1 to ζ=10. The effect of infrared absorption is included.

$$T^{max} = \frac{Q\exp(-1/2)}{\sqrt{2\pi}}\zeta^{-1} \quad . \tag{33}$$

The decrease in the thermal signal will be

$$\frac{T_2^{max}}{T_1^{max}} = \frac{\zeta_1}{\zeta_2} \tag{34}$$

or by a factor of about 250 for the current case. The resolution increases as $\sqrt{\zeta}$ but the signal decreases as ζ.

Therefore, to detect the signal at a depth ζ equally well as another one near the surface, the number of sampling points must increase proportionally to ζ. This means that the spacing of internal points should not be uniform: the internal points should be more closely spaced near the surface of the sample. This may be achieved by letting the spacing increase geometrically

$$\zeta_{i+1} = (1 + \alpha)^i \zeta_1 \tag{35}$$

where α is a positive constant that will depend on the number of internal points to be calculated, the depth of the shallowest point, and the depth of the deepest point. The characteristic time that corresponds to the *i*th depth is

$$\tau_c = \frac{(1+\alpha)^{2i}\zeta_1^2}{2} \tag{36}$$

Note that the ζ_i's will be distributed uniformly when plotted on a logarithmic scale.

The final depth may be determined according to the last sampling time or using Figure 5. This shows the magnitude of the maximum signal reaching the surface for subsurface planar impulses of equal magnitude. By the time the impulse has reached a depth of $\zeta = 100$, the maximum signal has dropped by a factor of over 200. This was somewhat arbitrarily chosen as the deepest ζ_N. The first depth ζ_1 is based on the first available sampling interval. The factor α is readily determined as

$$\alpha = \left[\frac{\zeta_N}{\zeta_1}\right]^{\frac{1}{N-1}} - 1 \tag{37}$$

once the number of internal temperature points to be calculated has been chosen.

4. METHOD

Conversion of surface temperatures to initial temperatures was evaluated in two ways. The first method employed exact analytic solutions to generate test data having known solutions; the second method used an optical glass filter with known optical and thermal properties to test the method with real data. Lastly, the conversion method was applied to a preliminary set of *in vivo* skin-tanning data to evaluate the internal production of melanin.

All data (numerical, filter or skin) was inverted identically except for two minor changes. The first was that the diffusivity of the filter was assumed to be equal to that of glass and not that of water (i.e., 0.0058 and not 0.0014 cm^2/s). The second involved the Marquardt-Levenberg factor λ; the numerical experiments used λ = 0.008, the filter experiments used λ = 0.02 and the skin data used λ = 0.05. The increase in the size of λ indicates that more smoothing was required for the experimental data than for the computer generated data.

The inversion process normalized the radiometric signal and averaged the data as

described above to achieve 40 values uniformly spaced logarithmically in time between 1 microsecond and 1 second. The number of internal temperature points generated was either 20 or 40 and were also distributed uniformly on a logarithmic scale between 1 and 1000 μm.

4.1 Computer Simulation

All numerical data assumed that the diffusivity was equal to that of water and that the infrared absorption coefficient was 1200 cm^{-1}. The kernel matrix was calculated using Eq. (15). For all sets of data, 400 normalized surface temperatures were generated uniformly distributed between 0 and 1 second. Three different sets of numerical data were generated: a planar impulse, two layers, and exponential temperature distributions.

The radiometric signals for an instantaneously heated unit planar impulse at depths of 5, 10, 50, 100, and 500 μm were generated. The function used to generate the signals as a function of time for the planar impulses was that of Eq. (14),

$$s(\tau) = K_{\text{plane}}(\zeta_0, \tau) \tag{38}$$

where ζ_0 was the depth of the planar source.

The signals for two 50 μm layers were generated next. The first layer had its top located 100 μm deep and the second one was located 200, 400, or 800 μm deep. The surface temperature for the two layered sources used a combination of superposition and Eq. (15). The signal from each layer was generated using

$$s(\tau) = h(\zeta_{\text{bottom}}, \tau) - h(\zeta_{\text{top}}, \tau) \tag{39}$$

where h is defined in Eq. (16), ζ_{top} is the location of the top of the layer, and ζ_{bottom} is the depth of the bottom of the layer. The responses for both layers were added together using the principle of superposition.

Three exponential distributions associated with absorption coefficients of 10, 30, and 100 cm^{-1} were used. The temperature distribution for the homogeneous absorbing medium assumed a normally incident pulse of light. The initial temperature distribution is

$$f(\zeta) = T(\zeta, 0) = \frac{E_0 \mu_a}{\rho c} \exp(-\gamma \zeta) \tag{40}$$

where $\gamma = \mu_a / \mu_{IR}$, E_0 is the radiant exposure reduced by any losses due to specular reflection from the surface, ρc is the volumetric specific heat of the sample, and μ_a is

the optical absorption coefficient at the incident light wavelength. All absorbed light is assumed to be converted to heat. Substituting this distribution into Eq. (6), and using Green's function for a planar adiabatic source [13] yields

$$s(\tau) = \frac{\gamma}{1-\gamma^2}[\exp(\gamma\tau)\mathrm{erfc}(\sqrt{\gamma\tau}) - \gamma\exp(\tau)\mathrm{erfc}(\sqrt{\tau})] \qquad (41)$$

after suitable normalization to the incident radiant exposure and the initial temperature.

4.2 Glass Filter Experiments

The glass filter experiments were performed using a microsecond pulsed dye laser (Palomar Medical) operating at 506 nm. The light was incident on the sample at an angle of 45°. The spot size was about 5mm in diameter. A Dow-Corning OG 590 glass filter served as the target and had an absorption coefficient at 590 nm of 90cm^{-1}. The diffusivity of the filter was assumed to be 0.0058 cm^2/s. PPTR experiments of the filter alone or the filter covered with one or more 150 μm thick microscope cover slips were made. Good thermal contact between the cover slip and the filter was ensured by using a drop of water.

Figure 1 shows a schematic diagram of the experimental arrangement. The infrared thermal signal was monitored using a HgCdTe detector (EG&G Judson) with a range of 8–12 µm. The 1 mm^2 image spot was placed at the focal plane of a germanium lens telescope with a conjugate ratio of 1:1. The detector signal was conditioned using a DC to 1.5MHz amplifier impedance matched to the detector. The electrical response of the detector, after pre-amplification, was monitored with a digital oscilloscope and 512 data points were collected after the laser pulse every 50 µs. One pulse was used for these experiments.

4.3 Skin Experiments

The amount of UV radiation necessary to generate a sunburn was determined by exposing the skin of the inner forearm to a solar simulator. Ten separate 1 cm^2 spots were exposed to a series of ultraviolet doses starting at 20 mJ/cm^2. These were increased by 30%, to achieve a series of doses of 20, 26, 34, 44, ..., 163 mJ/cm^2. The dose corresponding to the site with minimal perceptible redness was identified as the minimum erythema dose.

A site 5cm × 5cm on the opposite inner forearm was exposed to twice the minimum erythema dose to illicit a sunburn, followed by tanning. PPTR experiments

were performed using a microsecond pulsed dye laser (Candela SLL-500) operating at 627 nm on days 1, 2, 5, 12, 23. This wavelength was chosen because the primary absorber at 627 nm is melanin [18]. A 5mm diameter laser spot on the skin was made at an incidence angle of 15°. The signal from HgCdTe detector (New England MPC 12-1-8) with a detection bandwidth of 3–12 μm was amplified and collected using a digital oscilloscope. Forty thousand data points were collected at a rate of 10 μs per point after the end of the laser pulse.

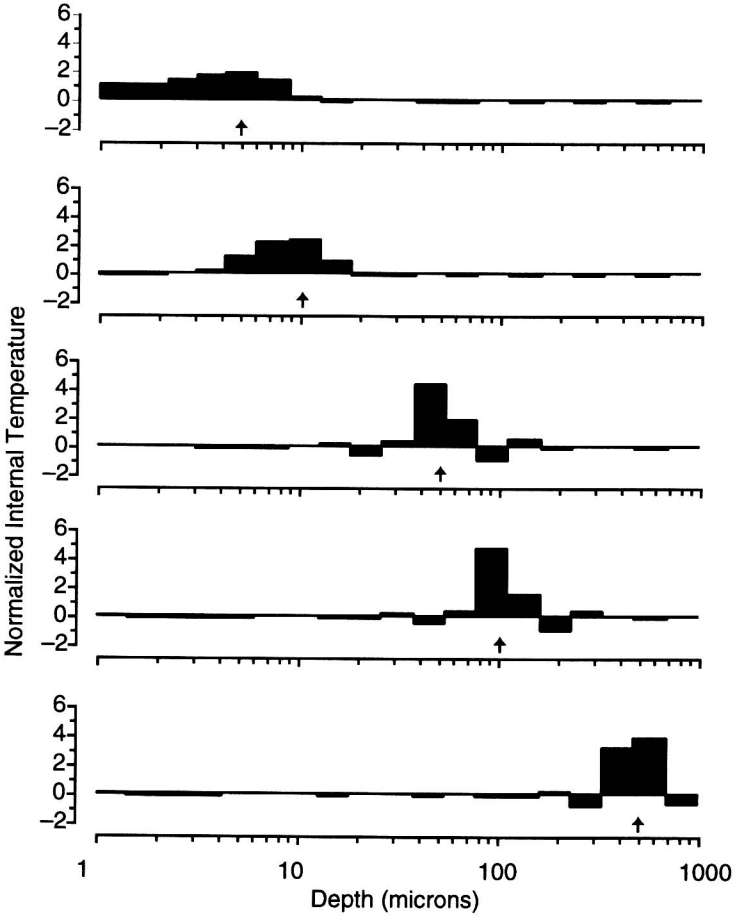

FIGURE 6. The calculated internal temperature distribution for pulses located at various depths as indicated by the arrows. The algorithm works well for identifying the depth of the impulse. The predicted width of the impulse increases with the depth.

5. RESULTS

5.1 Computer Simulations

The inversion of the computer simulations used 20 layers distributed uniformly on a logarithmic scale from 1 to 1000 μm. The Marquardt-Levenberg value used for all the computer generated data is $\lambda = 0.008$.

The first set of results is shown in Figure 6. The horizontal axis is chosen to be logarithmic to show the uniform distribution of layer thicknesses. Each histogram bar corresponds to one layer. The algorithm does a good job at roughly localizing the depth of the impulse, but only resolves the impulse to a region 2-4 layers thick.

The two-layer results are plotted on a linear depth scale in Figure 7. Again, the rough locations of both layers are good, but the exact width becomes larger with increasing depth. For example, the 100 μm peak is only 100 μm wide, compared to the 800 μm peak that is 300 μm wide. Notice that when the layers were located at 100–150 μm and 200–250 μm, they could not be distinguished.

The final set of computer data in Figure 8 shows excellent agreement between the calculated symbols and the expected lines. The data is plotted with a logarithmic vertical axis to make the exponential attenuation linear. The correspondence only begins to fail when the initial temperature drops below one-tenth the initial surface temperature.

5.2 Glass Filter

The results for the colored glass filter with and without a cover glass are shown in Figures 9 and 10. Stacking multiple cover slips on the glass filter generated detectable changes in the surface signal until a total of five cover slips were used.

5.3 Human Skin

The results for the skin tanning experiment are shown in Figure 11. The migration of melanin through the skin is evident. The slight depression in the data at about 8 μm is probably an artifact of the fitting process. Day 5 was omitted for clarity.

6. DISCUSSION

The inverse PPTR method presented in this chapter is fast and works with optically inhomogeneous media. The dispersive nature of thermal conduction severely constrains the depths that can be probed with this technique. The maximum change

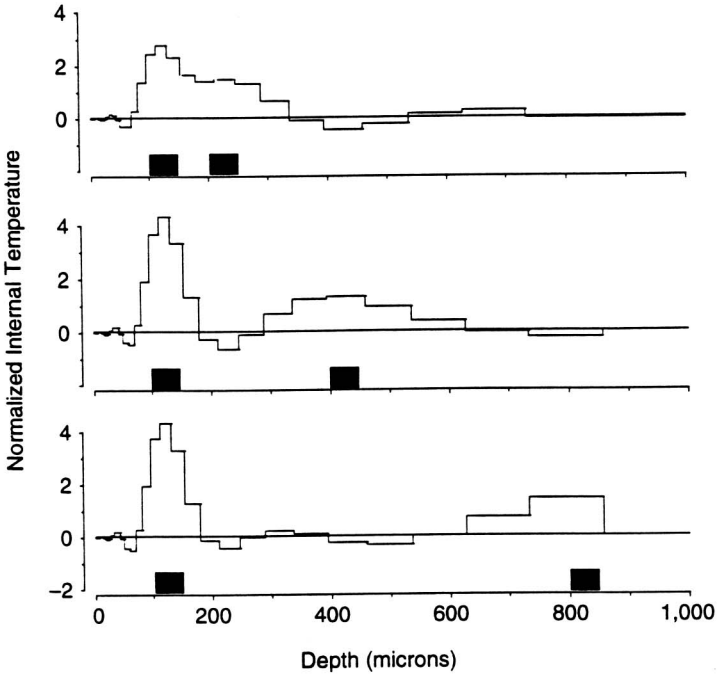

FIGURE 7. The calculated temperature distribution for two 50μm layers. One layer is located 100μm deep in each graph. The second layer is located at 200, 400, and 800μm. The location and width of each subsurface layer is indicated by the bars below each graph.

in radiometric signal at the surface becomes very small very quickly. Currently, the method is practical for subsurface layers less than 500 μm deep. The method is based on a readily available package for matrix manipulation (singular value decomposition). The tremendous amount of data collected during a PPTR experiment is reduced using a "sliding averaging scheme."

Negative temperatures were generated in some of the test cases. These are unphysical, but were intentionally included to emphasize a deficiency of this algorithm. One simple solution is to set the negative temperatures equal to zero and proceed. More sophisticated approaches, for example using non-negative least squares [17] or other constraints on the least-squares process will avoid such problems. It is noteworthy that nearly all the negative temperatures generated are associated with a rapid change in the internal temperature, or with large depths. Such changes are likely to create havoc with any fitting process, and the negative temperatures are a good indication when the algorithm is not working.

This technique is very fast. Once the initial singular value decomposition of the kernel has been accomplished and a particular value for λ has been selected, the initial temperature distribution is generated by a single matrix multiplication. The choice of the times for the surface signals and the number of signals that are averaged allows an initial set of data containing perhaps 40,000 data points to be reduced to only 40.

This also helps to reduce measurement noise for the later points.

No attempt was made to add pseudo-random noise to the generated surface temperatures because preliminary investigations showed that the Marquardt-Levenberg smoothing process excelled at removing white and Gaussian noise. Instead, real experiments with real noise were included. The inversion algorithm did not work nearly as well with the colored glass filter data as it did with numerically generated data. This may have been the result of surface contamination of the glass filter or because an improper value for the infrared penetration was assumed for the glass — it was assumed to be the same as that for water (1200 cm^{-1}).

This inversion technique is not suitable for resolving two absorbing layers relatively close together. Based on the impulse response results, it seems that a good rule of thumb is to expect a resolution about equal to the depth, i.e., about 10 μm at a depth of ten microns and 400 μm at a depth of four hundred microns. However, despite this limitation, PPTR has promise for non-invasively investigating the first 500 μm or so of tissue.

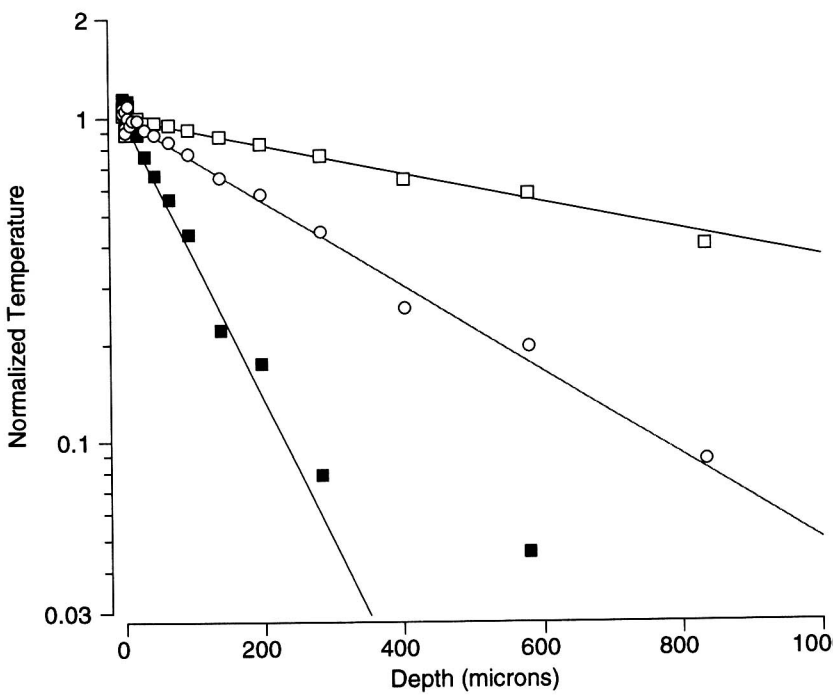

FIGURE 8. The calculated temperature distribution for three absorbing-only samples. The predicted temperatures work well as long as the predicted temperature is greater than one-tenth the maximum temperature.

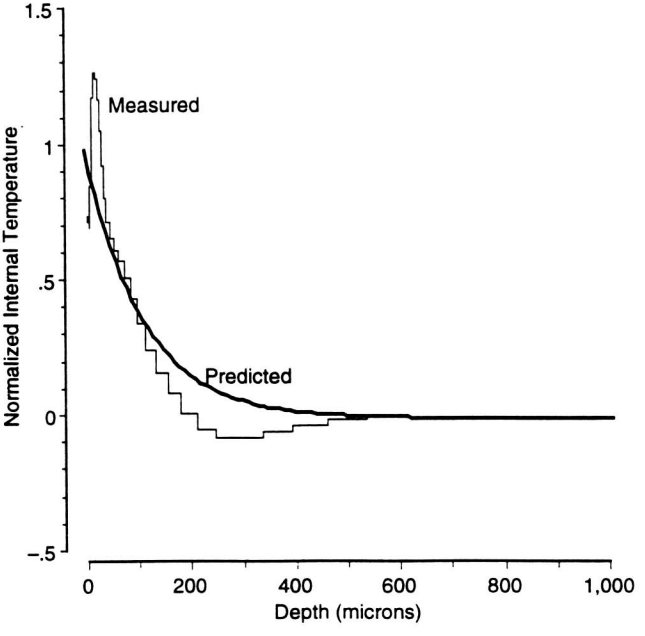

FIGURE 9. The calculated and measured temperature distributions for a glass absorbing filter.

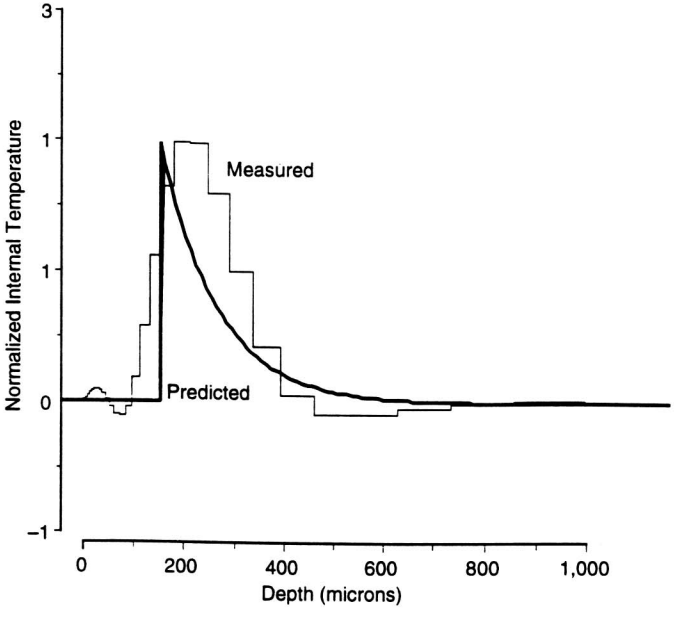

FIGURE 10. The calculated and measured temperature distributions for a glass absorbing filter covered by a 150μm thick microscope cover slip.

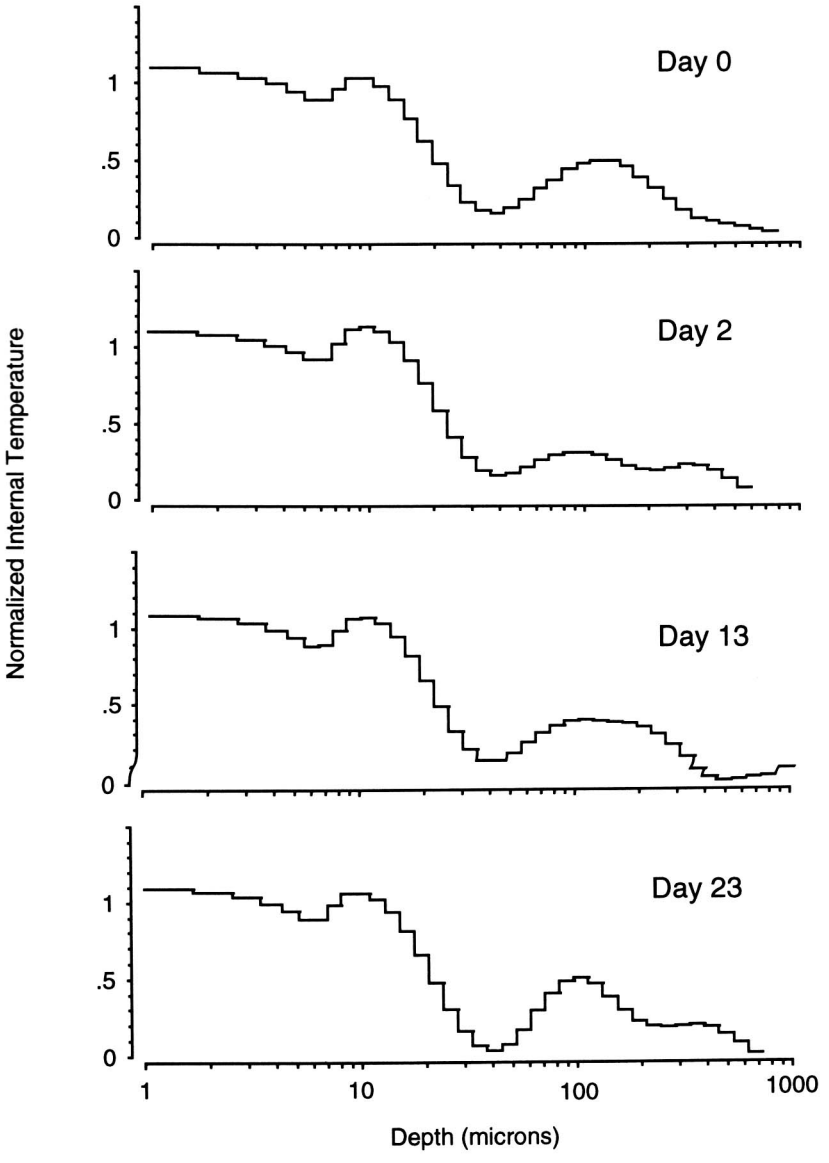

FIGURE 11. The calculated temperature distribution due to 630-nm laser light on a sunburned area of skin on various days after the ultraviolet exposure.

REFERENCES

1. Blank, I.H., Moloney, J., Emslie, A.G., Simon, I., and Apt, C., *J. Invest. Dermatol.* **82**, 188–194 (1983).
2. Tam, A.C., and Sullivan, B., *Appl. Phys. Lett.* **43**, 333–335 (1983).
3. Leung, W.P., and Tam, A.C., *Opt. Lett.* **9**, 93–95 (1984).
4. Leung, W.P., and Tam, A.C., *J. Appl. Phys.* **56**, 153–161 (1984).
5. Imhof, R.E., Birch, D. J.S., Thornley, F.R., Gilchrist, J.R., and Strivens, T.A., *J. Phys. E: Sci. Instrum.* **17**, 521–525 (1984).
6. Tam, A.C., *Infrared Phys.* **25**, 305–313 (1985).
7. Prahl, S.A., Vitkin, I.A., Bruggemann, U., Wilson, B.C., and Anderson, R.R., *Phys. Med. Biol.* **37**, 1203–1217 (1992).
8. Long, F.H., and Deutsch, T.F., *IEEE J. Quantum Electron.* **QE-23**, 1821–1826 (1987).
9. Long, F.H., Nishioka, N.S., and Deutsch, T.F., *Lasers Surg. Med.* **7**, 461–466 (1987).
10. Anderson, R.R., Beck, H., Bruggemann, U., Farinelli, W., Jacques, S., and Parrish, J. A., *Appl. Opt.* **28**, 2256–2262 (1989).
11. Balageas, D.L., Krapez, J.C., and Cielo, P., *Appl. Opt.* **59**, 348–357 (1986).
12. Long, F.H., Anderson, R.R., and Deutsch, T.F., *Appl. Phys. Lett.* **51**, 2076–2078 (1987).
13. Vitkin, I.A., Wilson, B.C., and Anderson, R.R., *Appl. Opt.* **34**, 2973–2982 (1995).
14. Prahl, S.A., Bruggemann, U., and Anderson, R R., in *Proceedings of Lasers in Dermatology and Plastic Surgery*. SPIE 1992 (abstract).
15. Jacques, S.L., Nelson, J.S., Wright, W.H., and Milner, T.E., *Appl. Opt.* **32**, 2439–2446 (1993).
16. Carslaw, H.S., and Jaeger, J.C., *Conduction of Heat in Solids 2nd ed.*, Clarendon Press, Oxford, (1986).
17. Lawson, C.L., and Hanson, R.J., *Solving Least Squares Problems*, Prentice-Hall (1974).
18. Anderson, R.R., and Parrish, J.A., in Regan, J.D. and Parrish, J.A., editors, *The Science of Photomedicine*, Plenum Press, New York (1982).